RSC Advances

PAPER

View Article Online
View Journal | View Issue

Cite this: *RSC Adv.*, 2017, **7**, 48649

Insight into the structure evolution and the associated catalytic behavior of highly dispersed Pt and PtSn catalysts supported on $La_2O_2CO_3$ nanorods†

Fengjun Hou,[ab] Huahua Zhao,[a] Huanling Song,*[a] Lingjun Chou,*[ac] Jun Zhao,[a] Jian Yang[a] and Liang Yan[a]

The current work introduces highly dispersed Pt and PtSn catalysts supported on $La_2O_2CO_3$ nanorods prepared *via* ultrasonic impregnation, which are used as probe catalysts for the liquid-phase crotonaldehyde hydrogenation. The physicochemical properties of the catalysts are assessed by means of various techniques, including XRD, TEM, XPS, H_2-TPD, *in situ* CO-DRIFT and X-ray adsorption fine structure (XAS). A close combination of catalyst surface experiments and the reactive performances reveals that the distinct reactive performance of the Pt and PtSn catalysts is tentatively attributed to the composition-dependent architecture of Pt–lanthanum interfaces and bimetallic particles while excluding the particle size effect. Catalytic activity tests demonstrate that incorporation of Sn into Pt catalyst brings great significance to the selective hydrogenation of carbonyl groups as it results into the structure evolution of bimetallic particles. An optimization of Sn loading and reaction conditions achieves a 5-fold and 7-fold improvement in the selectivity and yield to crotyl alcohol over the parent Pt catalyst. Lastly, it is found from the catalyst reusability study that metal particles of PtSn catalysts suffers easily from particle migration and growth compared to the Pt catalyst, most likely resulting from a weaker metal–support interaction.

Received 10th September 2017
Accepted 9th October 2017

DOI: 10.1039/c7ra10084a

rsc.li/rsc-advances

1. Introduction

Unsaturated alcohols are widely employed as important intermediates for the production of fragrances and pharmaceuticals, and can be attained by the chemoselective hydrogenation of unsaturated aldehydes.[1] However, this selective hydrogenation process is challenging since the hydrogenation of the carbonyl group is thermodynamically unfavorable over the olefinic bond.[2] To circumvent this issue, significant efforts have been devoted to the development of effective catalysts with superior carbonyl selectivity. For another, crotonaldehyde (CRAL) hydrogenation has been also studied as a model reaction to probe the catalyst surface and active sites of heterogeneous catalysts.[3–8] Among them, platinum is one of the most exploited metals for its ability to easily capture and dissociate hydrogen. Regardless of the high activity, the limited selectivity to the desired product is one of the main problems for CRAL hydrogenation over the Pt catalysts.

Heteroatoms of Pt and a transition metal (M = Fe, Co, Ge or Sn) are reported to perform high selectivity towards unsaturated alcohols and produce changes in the reactivity.[9–14] The promotion effect of M on the catalytic behavior of Pt catalyst can be generally interpreted in terms of geometric (dilution of Pt sites by PtM alloys or MO_x species) or electronic (the electron density of Pt) aspects. A plot of reaction selectivity to cinnamyl alcohol from cinnamaldehyde hydrogenation *versus* the first row of transition metals as dopers of Pt gave a typical volcano shape curve, which is proposed to be derived from the difference in *d*-band center position from the Fermi level when the Pt surface is electronically modified by the transition metal.[15] In addition, the composition variation is reported to induce changes in the particle size and structure of bimetallic nanoparticles (NPs). Rong *et al.* reported the structure evolution of PtSn NPs from the SnO_{2-x}-patched PtSn alloy to the SnO_{2-x}-patched Pt cluster as the Sn/Pt ratio increases, accompanied by an increase in the particle size, improving the desired selectivity for CRAL hydrogenation.[16] In this sense, various preparative methods, *e.g.* atomic layer deposition (ALD) and surface organometallic chemistry (SOMC), have been adopted to precisely control the architecture of bimetallic NPs.[17,18] However, it is still difficult to obtain homogeneous composition and structure of bimetallic

[a]*State Key Laboratory for Oxo Synthesis and Selective Oxidation, Lanzhou Institute of Chemical Physics, Chinese Academy of Sciences, Lanzhou 730000, PR China. E-mail: ljchou@licp.cas.cn; songhl@licp.cas.cn; Fax: +86 931 4968 129; Tel: +86 931 4968 066*

[b]*University of Chinese Academy of Sciences, Beijing 100049, PR China*

[c]*Suzhou Research Institute of LICP, Chinese Academy of Sciences, Suzhou 215123, PR China*

† Electronic supplementary information (ESI) available. See DOI: 10.1039/c7ra10084a

NPs in consideration of their sensitivity to the synthetic parameters.

Besides, support plays a crucial role in the chemical composition and structure of active metal, and therefore influences the catalytic behavior of its supported catalyst. In this case, developing of Pt or PtM crystals on an active support is one of the most common strategies adopted to improve the unsaturated alcohol yield. Novel carbon materials (CNTs, CNFs, OMCs, RGOs) and reducible oxides (TiO_2, CeO_2, FeO_x), are usually employed as supports and demonstrated to enhance the selectivity towards the carbonyl hydrogenation.[8,13,19–23] The new catalytic sites located at the metal–support interface, involving either reduced cations or oxygen vacancy sites, are reported to activate the carbonyl bond and increase the desired selectivity.[22,23]

Since studies on its coke inhibition and impressive activity for oxidative coupling of methane (OCM) are reported, lanthanum oxy-carbonate ($La_2O_2CO_3$) receives considerable attention.[24,25] As far as we know, $La_2O_2CO_3$ materials with specific morphology are scarcely studied in the hydrogenation process, although they are widely employed as important ingredients of heterogeneous catalysts in oxygen reduction reaction, steam reforming of glycerol and biofuel production because of their unique hydrotalcite-like structure and abundant active oxygen species.[26–29] In our previous work, preferential deposit of Pt on the {101} facets of $La_2O_2CO_3$ nanorods (denoted as Pt/LOC) is accounted for its superior reactive performance for CRAL hydrogenation to the Pt randomly dispersed on the particle-shaped counterpart.[30] Herein we carry out a systematic study on the physicochemical properties and the associated catalytic behavior of PtSn catalysts. An ultrasonic impregnation procedure is used to synthesize well-dispersed Pt and PtSn NPs on the support. The chemical composition and structure of the catalysts are elaborately analyzed by a series of techniques. Catalytic activity tests for CRAL hydrogenation are performed as a probe reaction to discern the structure-activity correlation of PtSn catalysts with varying Sn/Pt molar ratios.

2. Experimental

2.1 Catalysts preparation

$La_2O_2CO_3$ powders and nanorods was obtained by annealing the lanthanum hydroxide nanostructures at 500 °C for 3 h.[30] $La_2O_2CO_3$ powders and nanorods has specific surface area of 103 $m^2\ g^{-1}$ and 45 $m^2\ g^{-1}$, which is calculated based on the Brunauer–Emmett–Teller (BET) method in the relative pressure range of 0.05–0.30.

All catalysts were fabricated *via* an ultrasonic impregnation procedure. The Pt/LOC was obtained from the mixture of $H_2PtCl_6\cdot 6H_2O$ ethanol solution (1.13×10^{-3} g_{Pt} mL^{-1}, 9 mL) and the support (1.0 g) with ultrasonic treatment for 30 min. This mixture was kept standing for 12 h, and then evaporated at 60 °C to remove the excessive solvent. Obtained powder was air-dried at 120 °C overnight, calcinated at 400 °C for 2 h, and thereafter reduced at 600 °C for 1 h under a flowing gas mixture of 20% H_2/N_2 (v/v). The nominal loading of Pt was 1.00 wt%.

The PtSn catalysts with different Sn/Pt molar ratios were prepared by the impregnation of the air-dried Pt/LOC (1.0 g) with $SnCl_2\cdot 2H_2O$ (0.0080 g, 0.0120 g or 0.0180 g) following an identical process. As determined by inductively coupled plasma optical emission spectrometry (ICP-OES) analyses (Table 1), Pt content of the prepared catalysts is in the range of 0.99–1.11 wt%; Sn content is 0.46 wt%, 0.57 wt%, and 0.87 wt%, corresponding to the Sn/Pt molar ratio of 0.69, 0.94, and 1.33; hence, the PtSn catalysts are denoted as $PtSn_{0.69}$/LOC, $PtSn_{0.94}$/LOC and $PtSn_{1.33}$/LOC, respectively. In addition, the PtSn catalyst supported on the $La_2O_2CO_3$ powders ($PtSn_{0.94}$/LOC-NP) and the PtSn catalyst prepared by conventional impregnation method without ultrasonic treatment ($PtSn_{0.94}$/LOC-CI) are fabricated for comparison.

2.2 Catalyst characterization

The amount of Pt and Sn was determined by ICP-OES on an Agilent 725-ES.

X-ray diffractograms (XRD) was performed on X'Pert Pro Multipurpose diffractometer (PANalytical, Inc.) with Cu Kα radiation (0.15406 nm) at room temperature from 10 to 80°. Measurements were conducted using a voltage of 40 kV, current setting of 20 mA, step size of 0.021, and count time of 4 s.

Sample morphology and dispersion was observed on the TECNAI G2 F20 high-resolution transmission electron microscopy under a working voltage of 200 kV. Sample preparation involved ultrasonic dispersion of the sample in ethanol and deposition of the mixture on a carbon-coated copper grid. The particle size distributions (PSD) were estimated by measuring at least 300 particles from several TEM micrographs for each sample.

Temperature programmed desorption of hydrogen (H_2-TPD) was taken on a ChemBET Pulsar TPR/TPD analyzer (Quantachrome

Table 1 Physicochemical properties of the samples measured by ICP-OES and H_2-TPD

				Amount of desorbed hydrogen[b] (μmol g_{Pt}^{-1})			
Catalyst	wt% Pt[a]	wt% Sn[a]	Sn/Pt[a]	Peak 1	Peak 2	Peak 3	Total
Pt/LOC	1.11	—	—	1.46(355)	0.58(404)	1.33(456)	3.37
$PtSn_{0.69}$/LOC	1.09	0.46	0.69	1.30(350)	0.64(406)	1.19(449)	3.14
$PtSn_{0.94}$/LOC	0.99	0.57	0.94	1.12(341)	0.63(402)	0.92(437)	2.67
$PtSn_{1.33}$/LOC	1.08	0.87	1.33	0.74(344)	0.63(413)	0.51(456)	1.87

[a] From the ICP-OES analyses. [b] From the H_2-TPD measurement.

Instruments U.S.) equipped with a TCD detector. 50 mg of reduced catalyst was loaded in a U-tube quartz reactor and pretreated at 400 °C for 1 h with Ar flushing to remove the impurities. The TPD experiment was carried out by heating the furnace to 900 °C at a ramp of 20 °C min^{-1} in flowing Ar (40 mL min^{-1}) after hydrogen-adsorption at 30 °C for 60 min.

X-ray photoelectron spectroscopy (XPS) was conducted on a Thermo Scientific ESCALAB250xi spectrometer to determine the surface atomic composition and chemical states of the catalysts. All binding energies were referenced to C 1s hydrocarbon peak at 284.8 eV. The spectra of each element were deconvoluted with a curve fitting routine in XPSPEAK41 software. Curve fitting of the Pt 4f, Sn 3d and O 1s spectra for the catalysts was performed after subtracting the background and fitting with the least squares best fitting routine, assuming an 80/20 Gaussian/Lorentzian product function.

The CO-DRIFT spectra of the samples were recorded on the BRUKER V70 Fourier transform infrared spectrometer equipped with an *in situ* infrared reaction device. Measurements were conducted using a spectral resolution of 4 cm^{-1}, step size of 20 kHz, and accumulation of 64 scans. Briefly, self-supporting pellet was prepared from the reduced sample and placed directly in the IR quartz cell equipped with KBr windows. The reduced sample was pretreated at 300 °C for 90 min in flowing H_2 followed by 30 min flushing in Ar. After pretreatment, the sample was cooling down to 40 °C. And then a gas mixture of 0.5% CO/Ar was admitted into the cell and left to equilibrate for 40 min. And then the CO-adsorption spectra of the sample were continuously recorded with 40 min flushing in Ar flow.

The Pt L_{III}-edge X-ray absorption spectroscopy (XAS) was measured at the 4W1B station of the Beijing Synchrotron Radiation Facility (BSRF). Experiments were performed at ambient temperature in transmission mode using a Si (111) solid state detector for selection of energy. The data reduction and process was performed using the ATHENA and ARTEMIS software.[31] Each EXAFS function (χ) was attained by subtracting the post-edge background from the overall absorption and then normalized relating to the edge jump step. Then, k^3-weighted EXAFS oscillation in the k-space for Pt L_{III}-edge, were Fourier transformed (FT) to the r-space to isolate the EXAFS contributions from different coordination shells. The Pt–Pt scattering path was used in the fitting of Pt foil; the Pt–O and Pt–Pt scattering paths were used in the fitting of the Pt/LOC; the Pt–O, Pt–Pt and Pt–Sn scattering paths were used in the fitting of the $PtSn_x$/LOC samples. The structural parameters, such as the coordination number CN, the inter-atomic distance R, the Debye–Waller factor σ^2, and the edge-energy shift ΔE_0, were allowed to vary during the fitting process.

2.3 Catalytic test

The catalytic behavior for liquid-phase CRAL hydrogenation was operated in a 100 mL Parr reactor. 100 mg of catalyst, 1 mL of CRAL and 19 mL of ethanol was charged into the autoclave. The autoclave was purged three times and then pressurized with H_2. The reaction was heated to the desired temperature for reaction with vigorous stirring. The compositions of reactants and products were identified and analyzed on Agilent 7890A-5975C equipped with an FID detector. The catalytic activity and selectivity of the products was determined by using the internal normalization method with *n*-hexanol as internal standard. CRAL conversion ($Conv._{CRAL}$) was defined as the adductive percentages of CRAL converted into different products. The selectivity to a given product (i) was calculated as the ratio between the moles of product i and the total moles of products.

The catalyst reusability study was conducted under the optimization reaction conditions (T = 160 °C, p = 2.0 MPa, t = 60 min). Monometallic Pt/LOC and bimetallic $PtSn_{0.94}$/LOC were selected as the catalysts for reutilization test. The spent catalysts were regenerated from the mixture of hydrogenation system by rinsing with absolute ethanol, and drying overnight at 120 °C before activation in air at 300 °C for 1 h.

3. Results

3.1 Catalysts characterization

3.1.1 XRD patterns. XRD technique was adopted to study the crystalline phase of the catalysts, and the patterns are presented in Fig. 1. The diffraction signals of the Sn/LOC are in accordance with typical patterns of hexagonal $La_2O_2CO_3$ (JCPDS No. 25-0424). By contrast, Pt-involved catalysts show intensified diffraction signals, which can be indexed to a mixture of hexagonal $La_2O_2CO_3$ (JCPDS No. 25-0424) and hexagonal La_2O_3 (JCPDS No. 02-0688). Given that $La_2O_2CO_3$ has a hydrotalcite-like structure consisting of $(La_2O_2)^{n+}$ layers and CO_3^{2-} ions, incorporation of a noble metal onto the $La_2O_2CO_3$ surfaces may induce the phase transformation of lanthanum upon thermal treatment.[25,32] It is plausible to accept that the presence of La_2O_3 is related to the phase transformation of $La_2O_2CO_3$ catalyzing by Pt atoms at the Pt–lanthanum interfaces upon reduction, suggesting a strong metal–support interaction. It is noted that the

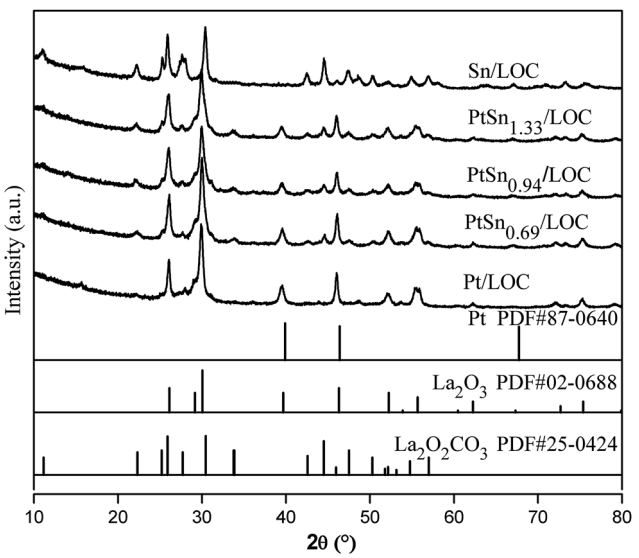

Fig. 1 Standard patterns of hexagonal $La_2O_2CO_3$, hexagonal La_2O_3 and cubic Pt crystalline. XRD patterns of the Pt/LOC, Sn/LOC and $PtSn_x$/LOC series catalysts.

phase transformation of $La_2O_2CO_3$ is much promoted over $PtSn_{0.69}$/LOC, as indicated by the increased phase composition of La_2O_3, assuming an increase in the number of individual Pt atoms possibly segregated from lanthanum surface. However, further increasing tin loading causes an obvious drop in overall peak intensities as a result of the passivation effect of tin on the catalyst surface. In addition, no reflection associated with metals or alloys is detected, presumably due to the small crystalline size and good dispersion of metals, which is confirmed by the following TEM images.

3.1.2 TEM images. As shown in Fig. 2a, LOC displays diameters of 15–20 nm and lengths of 200–400 nm. The particle size and dispersion of metals on the catalysts estimated by TEM images are displayed in Fig. 2b–e, which clearly shows that the rod-shaped morphology of lanthanum support is well maintained after the decoration of metals. A typical TEM micrograph of the Pt/LOC (Fig. 2b) demonstrates that uniform Pt NPs are highly dispersed on the catalyst surface and no agglomeration is observed even after reduction at 600 °C. Fig. 2f shows the histogram of particle sizes measured from the TEM images, indicating that Pt NPs in the reduced Pt/LOC have an average particle size of 1.4 nm. As clearly seen from Fig. 2c–e, the tin addition does not practically affect the size distribution of metal particles compared to the Pt/LOC. By contrast, Fig. S1† shows an obvious increase of metal particle size over the $PtSn_{0.94}$/LOC-CI (4.2 nm) and $PtSn_{0.94}$/LOC-NP (3.3 nm). It is evident that the employment of lanthanum nanorods and ultrasonic impregnation process plays a decisive role in controlling over the highly dispersed metal particles at a confined size range, which makes it feasible to probe the composition-dependent properties of the $PtSn_x$/LOC series catalysts while excluding the particle size effect.

3.1.3 XPS spectra. XPS measurement was conducted to analyze the surface composition and chemical states of the catalyst surface; the results are presented in Fig. 3 and Table 2. The Pt $4f_{7/2}$ and Pt $4f_{5/2}$ lines for the Pt/LOC exhibit a distinct

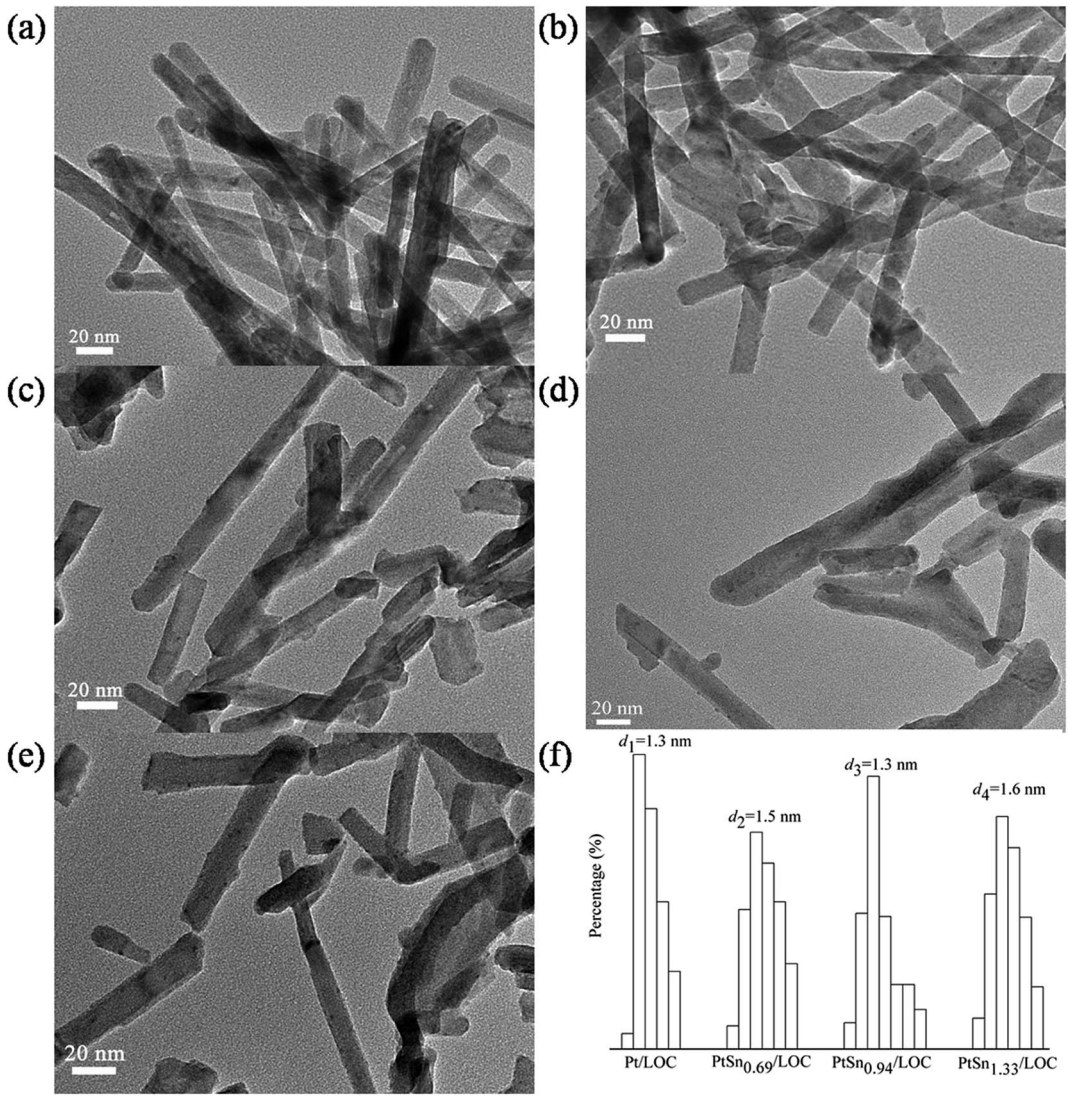

Fig. 2 Typical TEM images of (a) LOC, (b) Pt/LOC, (c) $PtSn_{0.69}$/LOC, (d) $PtSn_{0.94}$/LOC and (e) $PtSn_{1.33}$/LOC, (f) histograms showing the size distributions of metal particles over the catalysts.

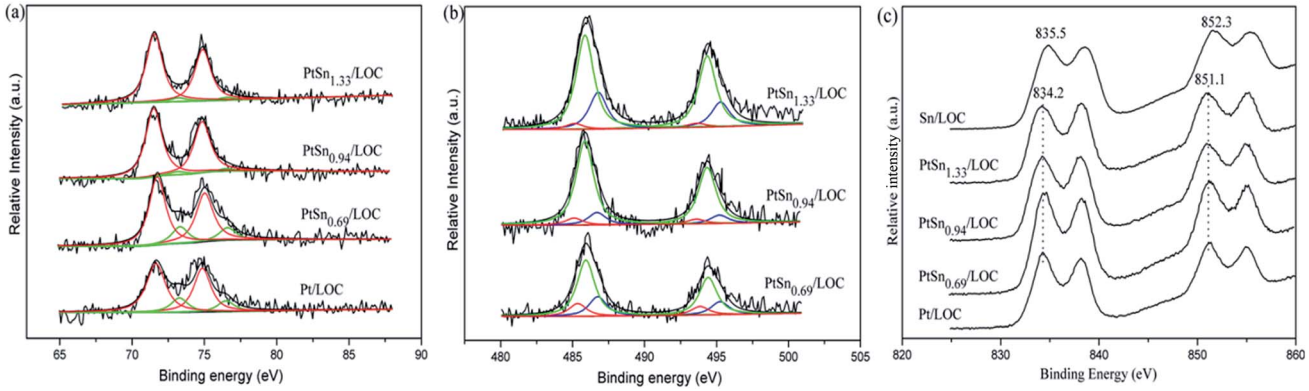

Fig. 3 XPS spectra of (a) Pt 4f, (b) Sn 3d, (c) La 3d for the samples. The curve fitting of the Pt 4f and Sn 3d spectra for the samples are performed using the XPSPEAK41 software according to the uniform constraints on the fitting parameters after subtracting the background.

Table 2 Chemical composition and valences of the catalysts determined by XPS measurement

Sample		Species	Binding energy (eV)	Pt^{2+}/Pt^0 or $Sn^0/(Sn^{2+} + Sn^{4+})^a$	Pt/La[b]	Sn/Pt[c]	O/La[d]
Pt/LOC	Pt $4f_{7/2}$	Pt^0	71.7	0.26	0.020	0.00	3.19
		Pt^{2+}	73.3				
$PtSn_{0.69}$/LOC	Pt $4f_{7/2}$	Pt^0	71.6	0.25	0.014	1.60	2.60
		Pt^{2+}	73.3				
	Sn $3d_{5/2}$	Sn^0	485.4	0.17			
		Sn^{2+}	485.9				
		Sn^{4+}	486.8				
$PtSn_{0.94}$/LOC	Pt $4f_{7/2}$	Pt^0	71.5	0.05	0.016	1.95	2.59
		Pt^{2+}	73.2				
	Sn $3d_{5/2}$	Sn^0	485.1	0.07			
		Sn^{2+}	485.9				
		Sn^{4+}	486.7				
$PtSn_{1.33}$/LOC	Pt $4f_{7/2}$	Pt^0	71.5	0.06	0.015	2.67	2.50
		Pt^{2+}	73.2				
	Sn $3d_{5/2}$	Sn^0	485.2	0.04			
		Sn^{2+}	485.9				
		Sn^{4+}	486.8				

[a] Pt^{2+}/Pt^0: the atomic ratio of oxidized platinum (Pt^{2+}) to metallic platinum (Pt^0); $Sn^0/(Sn^{2+} + Sn^{4+})$: the atomic ratio of metallic tin (Sn^0) to oxidized tin ($Sn^{2+} + Sn^{4+}$). [b] The molar ratio of Pt to La. [c] The molar ratio of Sn to Pt. [d] The molar ratio of O to La.

asymmetric shape inclined toward high binding energies and the peak area ratio deviates from the theoretical value of 1.33, suggesting the multiple chemical states of Pt.[33] The peaks of reduced Pt/LOC at 71.7 eV and 73.3 eV are assigned to the Pt $4f_{7/2}$ electrons of Pt^0 and Pt^{2+} species, respectively. The oxidized platinum is related to Pt catalyst involving the chlorinated precursors, which helps platinum remain unreduced in the final catalysts.[19,34] As shown in Table 2, the Pt^{2+}/Pt^0 atomic ratio of the Pt/LOC and $PtSn_{0.69}$/LOC is 0.26 and 0.25, much higher than that of the $PtSn_{0.94}$/LOC (0.05) and $PtSn_{1.33}$/LOC (0.06), suggesting that the reducibility of Pt is greatly improved most likely resulting from the crippling Pt–lanthanum interfaces with increasing Sn loading.

As shown in Fig. 3b, the Sn $3d_{5/2}$ peaks can be deconvoluted into three features assigned to Sn^0, Sn^{2+} and Sn^{4+} species. It is found that large quantities of tin exist as oxidative status according to the curve-fitting results of the Sn $3d_{5/2}$ spectra. As expected, with higher Sn/Pt molar ratio, the Sn $3d_{5/2}$ signals are evidently intensified. The Sn/Pt atomic ratio for the PtSn catalysts assessed by XPS analyses is 1.60, 1.95 and 2.67, much higher than that from ICP results. This demonstrates a significant surface enrichment of tin presumably because the impregnation order leads to the partially covered Pt NPs by tin. Besides, the atomic ratio of $Sn^0/(Sn^{2+} + Sn^{4+})$ is higher for $PtSn_{0.69}$/LOC (0.17) than that for $PtSn_{0.94}$/LOC (0.07) and $PtSn_{1.33}$/LOC (0.04), suggesting that most of tin is hardly reduced to metallic Sn^0 and exists as SnO_x entities at high Sn loading.

The La 3d spectra for Pt-involved catalysts, as shown in Fig. 3c, contain peak at 834.2 eV and its accompanying satellite peaks that can be attributed to the electrons of La $3d_{5/2}$ for La_2O_3. The peak at higher value (835.5 eV) for Sn/LOC corresponds to the electrons of La $3d_{5/2}$ for $La_2O_2CO_3$. These results verify the phase evolution of lanthanum catalyzed by Pt atoms at

the Pt–lanthanum interfaces, which is consistent with the previously discussed XRD patterns. It is noteworthy that the O/La ratio decreases from 3.19 to 2.50 as Sn/Pt value increases. This suggests that a proportion of oxygen species on the catalyst surface or subsurface is consumed, producing more oxygen vacancies by the promotion effect of tin. According to above results, it can be inferred that the tin addition induces an interaction between both metals, which affects the redox property of Pt and Sn, generating the Pt–SnO_x entities; at the same time, more surface oxygen vacancies are produced due to the formation of Pt–SnO_x species.

3.1.4 H_2-TPD measurements. To assess the H_2-metal bonding sites, H_2 desorption *vs.* temperature for the catalysts in the temperature range of 100–900 °C was performed. As shown in Fig. 4, the TCD signals for bare LOC contains two peaks centered at 565 °C and 800 °C, respectively. The H_2-TPD profiles for Pt-containing catalysts show an analogous shape, which can be divided into three regions according to the desorption temperatures. The low-temperature region of 100–500 °C corresponds to hydrogen desorbed from the metal sites; the mid-temperature one (500–700 °C) is related to hydrogen desorbed from the catalyst surface/subsurface, most likely due to lanthanum polarization by interaction with vicinal Pt atoms; while the high-temperature one above 700 °C originates from the reductive decomposition of bulk lanthanum.

In the case of the Pt/LOC, three overlapped desorption peaks centered at 355, 404 and 455 °C, are assigned to weak, medium and strong bonding sites with hydrogen, respectively. Table 1 summarizes the H_2 desorption capacity (in μmol g_{Pt}^{-1}) of the prepared catalysts calculated on the categorized temperature below 500 °C. The hydrogen desorption capacity for the samples is followed in a decreasing order of $PtSn_{0.69}$/LOC (3.14 μmol g_{Pt}^{-1}) > $PtSn_{0.94}$/LOC (2.67 μmol g_{Pt}^{-1}) > Pt/LOC (2.30 μmol g_{Pt}^{-1}) > $PtSn_{1.33}$/LOC (1.87 μmol g_{Pt}^{-1}). It is known that Pt is the effective sites for hydrogen adsorption and dissociation, whereas tin oxides has a relatively low capacity for hydrogen activation, and therefore the hydrogen desorption behaviors can mostly be ascribed to the noble metal Pt. The calculated hydrogen desorption capacity reveals that tin deposit changes the exposure degree of surface Pt sites available for hydrogen chemisorption. At low Sn content, the dilution effect of Pt sites by tin prevails, favoring the exposure of Pt sites; while at high Sn content, the blocking effect of tin predominates and decreases the number of exposed Pt sites. Besides, incorporation of tin lowers the overall peak intensity, in particular for the mid-temperature peak, confirming the strong passivation of catalyst surface by tin.

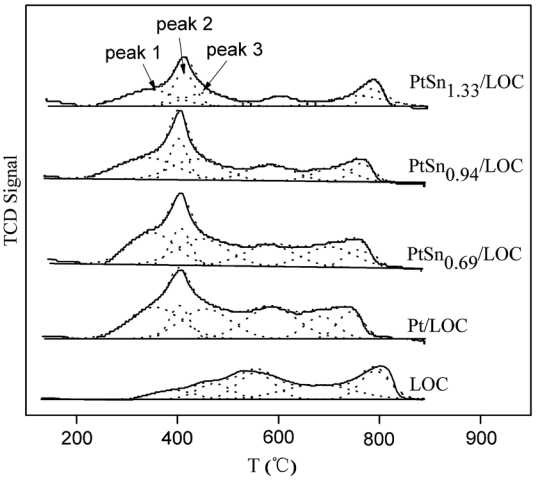

Fig. 4 H_2-TPD profiles of the samples.

3.1.5 CO-FTIR spectra. In order to probe the adsorption behavior of carbonyl groups on the catalyst surface, *in situ* CO-DRIFT spectroscopic investigation was conducted. As shown in Fig. 5, the spectra of fresh catalysts present three sets of peaks located at 2300–2400 cm^{-1}, 2150–2200 cm^{-1} and 2000–2100 cm^{-1}, which are assigned to gas phase CO_2, $CO_{(ad)}$ on lanthanum and linear-CO adsorption on low-coordinated Pt sites, respectively.[35,36] It is evident that addition of Sn into the Pt/LOC leads to a significant increase of the linear-CO signals on $PtSn_{0.69}$/LOC compared to the Pt/LOC, suggesting a dilution effect of Pt sites by tin. In comparison, the linear-CO signals for $PtSn_{0.94}$/LOC and $PtSn_{1.33}$/LOC are drastically decreased, most likely resulting from a decreasing number of surface Pt sites due to the passivation of catalyst surface by tin. These changes share similarities with the variations of XRD patterns and H_2-TPD profiles. In addition to the changes of peak intensity, it is observed that addition of Sn leads to a systematic red shift of the linear adsorbed CO signals. It is located at 2079 cm^{-1} for Pt/LOC, while 2074 cm^{-1} for $PtSn_{0.69}$/LOC, 2072 cm^{-1} for $PtSn_{0.94}$/LOC and 2069 cm^{-1} for $PtSn_{1.33}$/LOC. This indicates more back-donation of electrons from Pt to the 2p anti-bonding orbital of CO, suggesting an increased interaction between Pt and CO molecules.

It is proposed that the binding strength of CO on the Pt sites can somewhat reflect the adsorption of carbonyl group and desorption of the product.[37,38] The linear-CO adsorption on fresh Pt/LOC seems to be completely reversible as this band disappears when flushing with Ar for 24 min. By contrast, the linear-CO adsorption on the $PtSn_{0.69}$/LOC can be easily removed when flushing with Ar for 8 min; the linear-CO adsorption on the $PtSn_{0.94}$/LOC seems to be mostly desorbed on Ar flushing for 40 min; however, high tin concentration in $PtSn_{1.33}$/LOC does not result into noticeable changes of the linear adsorbed CO signals even after Ar flushing for 40 min. These results further manifest that the interaction between CO and Pt is greatly enhanced at high tin loadings. This enhanced binding force, on one hand, results into a chemisorption mode favoring the activation and hydrogenation of carbonyl groups on the metal Pt. On the other hand, it inhibits the product desorption and the recovery of active sites. In summary, the CO-DRIFT studies reveal that the coordination environment and exposure degree of Pt atoms in the catalysts is greatly changed upon tin addition; further, metal particles consist of Pt and Sn atoms leads to the composition-dependent variations in the interaction between CO and Pt. These two factors work together to determine the CO chemisorption behavior on Pt centers.

3.1.6 XAS spectra. To further study the electronic modification and the local environment of Pt, X-ray absorption spectroscopy (XAS) experiments were carried out on the reduced

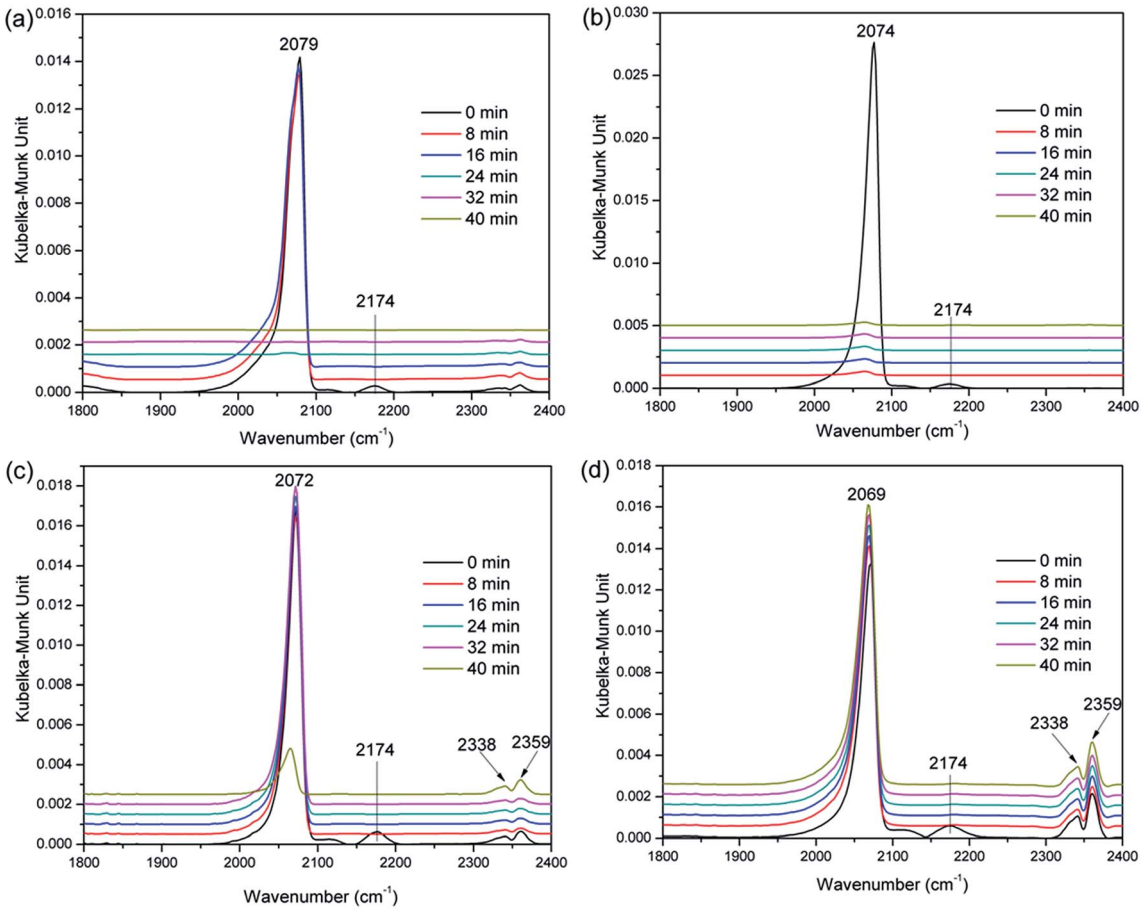

Fig. 5 DRIFT spectra of CO adsorbed on the prepared (a) Pt/LOC, (b) $PtSn_{0.69}$/LOC, (c) $PtSn_{0.94}$/LOC and (d) $PtSn_{1.33}$/LOC samples. The spectra were continuously recorded on the samples (50 mg) at 40 °C during Ar flushing for 40 min after introducing 0.5 Ar/CO for 40 min.

catalysts. X-ray adsorption near-edge spectroscopy (XANES) can provide crucial information on the electronic environments of the central absorbing atom. Fig. 6a presents the normalized Pt L_{III} edge XANES spectra of Pt foil and the catalysts. The white line at 11 570.3 eV ascribes to the $2p_{3/2}$ to 5d transition in Pt foil and is very sensitive to the average oxidation state of Pt. The white line intensities of the Pt-involved samples are higher than that of Pt foil, verifying the existence of positively charged Pt atoms that consists with the XPS results.[39,40] In the case of Pt-involved samples (the inset of Fig. 6a), XANES shifts to higher energy by 0.5 eV, and the region between 11 578 eV and 11 600 eV shows a different fine structure, which is indicative of a different geometry around the Pt atoms depending on the Sn/Pt ratios.

Fig. 6b shows the Fourier transforms (FTs) of k^3-weighted extended X-ray absorption fine structure (EXAFS) oscillations at the Pt L_{III}-edge. The main peaks of FTs for the catalysts located in the range of 2–3 Å can be assigned to the Pt–O, Pt–Pt or Pt–Sn contributions.[41] The structural parameters can be attained by curve-fitting the EXAFS data and summarized in Table 3. There is Pt–O bond at a distance of 2.02 Å for the Pt/LOC; its coordination number (CN) is 1.5. The contribution of Pt–O shell gives further evidence on the presence of oxidized Pt coordinated by oxygen atoms of lanthanum. In the case of bimetallic PtSn catalysts, the CN of Pt–O bond decreases to around 1.0, suggesting that some Pt atoms segregated from lanthanum surface are greatly reduced after the decoration of tin, in consistence with higher Pt^0/Pt^{2+} ratios for tin-promoted samples from XPS results.

For Pt/LOC, there is a Pt–Pt contribution at a distance of 2.72 Å, with an average CN of 5.9. By contrast, the CN of Pt–Pt bond for tin-promoted samples is continuously decreased to 4.2. The Pt–Pt bond of $PtSn_{0.94}$/LOC (2.62 Å) and $PtSn_{1.33}$/LOC (2.65 Å) shows shorter distance than that of Pt/LOC (2.72 Å) and $PtSn_{0.69}$/LOC (2.75 Å), suggesting the contraction of the bond distances owing to the formation of small Pt clusters at high Sn loading. In addition, the best fit for the third shell of $PtSn_{0.69}$/LOC is a Pt–Sn contribution at a distance of 2.66 Å, with an average CN of 1.1. The Pt–Sn contribution is greatly decreased to 0.3 for $PtSn_{0.94}$/LOC and 0.2 for $PtSn_{1.33}$/LOC, implying that a phase segregation of PtSn alloys occurs at high Sn loading. These changes give important clues on the structure evolution of bimetallic NPs from PtSn alloys to small Pt clusters with increasing Sn/Pt ratios.

It is found that the total CN of absorbing platinum atoms ($\Sigma N_{Pt\text{-}i}$) for Pt/LOC is 7.4, much higher than that for $PtSn_{0.69}$/LOC (7.2), $PtSn_{0.94}$/LOC (6.5), and $PtSn_{1.33}$/LOC (5.4). The decreased $\Sigma N_{Pt\text{-}i}$ values for tin-dopped samples lead to a hypothesis that a number of Pt atoms are neither directly

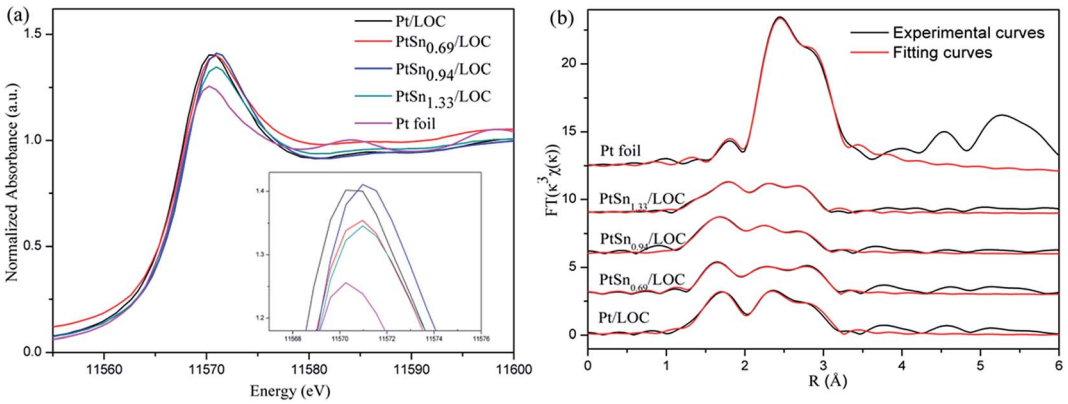

Fig. 6 (a) Normalized XANES spectra and (b) Fourier transforms (FTs) of Pt L_{III}-edge k^3-weighted EXAFS oscillations for Pt foil, Pt/LOC and $PtSn_x$/LOC catalysts.

Table 3 Structural parameters derived from curve fitting results of EXAFS oscillations at Pt L_{III}-edge

Sample	Shell	CN[a]	R (Å)[b]	ΔE_0 (eV)[c]	$\sigma^2 \times 10^{-3}$ (Å^2)[d]	R factor	$\Sigma N_{Pt\text{-}i}$[e]
Pt foil	Pt–Pt	12.0	2.76	8.0	4.57	0.001	12.0
Pt/LOC	Pt–O	1.5	2.02	10.9	3.47	0.008	7.4
	Pt–Pt	5.9	2.72	8.6	9.36		
$PtSn_{0.69}$/LOC	Pt–O	1.1	2.04	15.4	2.80	0.004	7.2
	Pt–Sn	1.1	2.66	−5.2	11.46		
	Pt–Pt	5.0	2.75	7.1	10.0		
$PtSn_{0.94}$/LOC	Pt–O	1.0	1.96	2.6	2.00	0.008	6.5
	Pt–Sn	0.3	2.57	14.3	2.32		
	Pt–Pt	5.3	2.62	2.2	9.00		
$PtSn_{1.33}$/LOC	Pt–O	1.0	2.03	12.0	5.00	0.006	5.4
	Pt–Sn	0.2	2.62	10.1	5.07		
	Pt–Pt	4.2	2.66	1.8	9.00		

[a] N: the average coordination number. [b] R: the interatomic distance. [c] ΔE_0: the inner potential shift. [d] σ^2: the Debye–Waller factor. [e] $\Sigma N_{Pt\text{-}i}$: the overall coordination number. The data range used for data fitting in k-space (Δk) and R-space (ΔR) are 2.0–10.7 Å^{-1} and 1.2–3.5 Å, respectively.

interacted with the Sn species nor with the support, presumably instead by forming the Pt–SnO_x entities through Pt–O–Sn bond. As revealed by the XPS results, more SnO_x entities with oxygen vacancy sites are produced at high tin loadings, which could be the probable reason for lower $\Sigma N_{Pt\text{-}i}$ values for the PtSn catalysts. Analogous results are previously discussed by Taniya on the tin-modified SiO_2-coated Pt catalyst.[38] In summary, the EXAFS analyses throw light on the structure evolution of bimetallic PtSn NPs with increasing Sn content. At low Sn concentration, the structure of $PtSn_{0.69}$/LOC is PtSn alloys patched by SnO_x entities; whereas at high Sn concentration, the structure of $PtSn_{0.94}$/LOC and $PtSn_{1.33}$/LOC is Pt clusters patched by SnO_x entities. The composition-dependent structure evolution of bimetallic NPs has also been observed on unsupported PtSn NPs and PtNi NPs.[41,42] As shown below, these Pt atoms diluted by PtSn alloy or SnO_x species exhibit distinct reactive behaviors for CRAL hydrogenation.

3.2 Reactive performance

3.2.1 Catalytic behavior in CRAL hydrogenation reaction. As shown in Fig. 7, CRAL is mainly hydrogenated to produce the desired unsaturated alcohol (crotyl alcohol, CROL), saturated aldehyde (butanal, BUAL), and saturated alcohol (butanol, BUOL). The main hydrogenation product distributions over the prepared catalysts are exhibited in Fig. 8. From the analysis of catalytic behavior, it is found that tin exerts great influence on the hydrogenation activity and carbonyl selectivity. The overall reactivity (γ_i) of 0.34 mmol g_{Pt}^{-1} s^{-1} over the Pt/LOC, corresponds to a CRAL conversion and CROL selectively of 66.2% and 14.1%, respectively. The reactivity of $PtSn_{0.69}$/LOC is improved to 0.59 mmol g_{Pt}^{-1} s^{-1}, accompanied by a steep increase in CRAL conversion (92.8%) and CROL selectivity (64.9%). It is noteworthy that an increased yield of alcohol products (CROL and BUOL), in contrast to the decreased saturated aldehyde (BUAL) selectivity, clearly demonstrates the additional activity to C=O hydrogenation for bimetallic systems. When the Sn/Pt ratio increases to 0.94, it reaches a maximum value of CROL selectivity (70.7%) at the expense of a slight decrease in the reactivity (0.51 mmol g_{Pt}^{-1} s^{-1}) and CRAL conversion (91.7%). Further increasing Sn content leads to a sharp drop in reactivity and CROL selectivity for $PtSn_{1.33}$/LOC. The CRAL conversions over the catalysts follows a decreasing order of $PtSn_{0.69}$/LOC > $PtSn_{0.94}$/LOC > Pt/LOC > $PtSn_{1.33}$/LOC. These results coincide

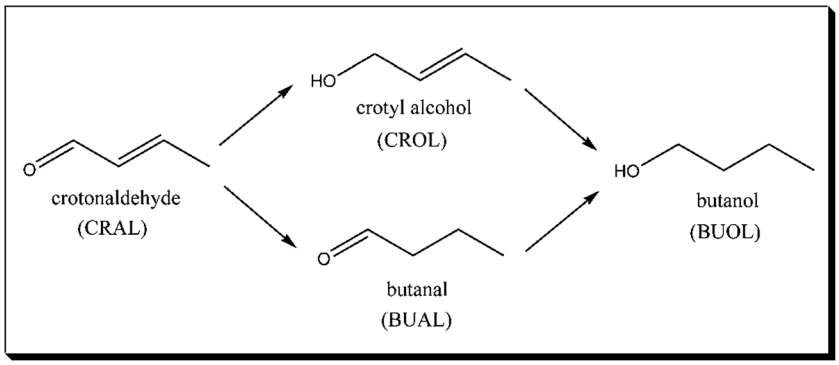

Fig. 7 The reaction diagram of CRAL hydrogenation.

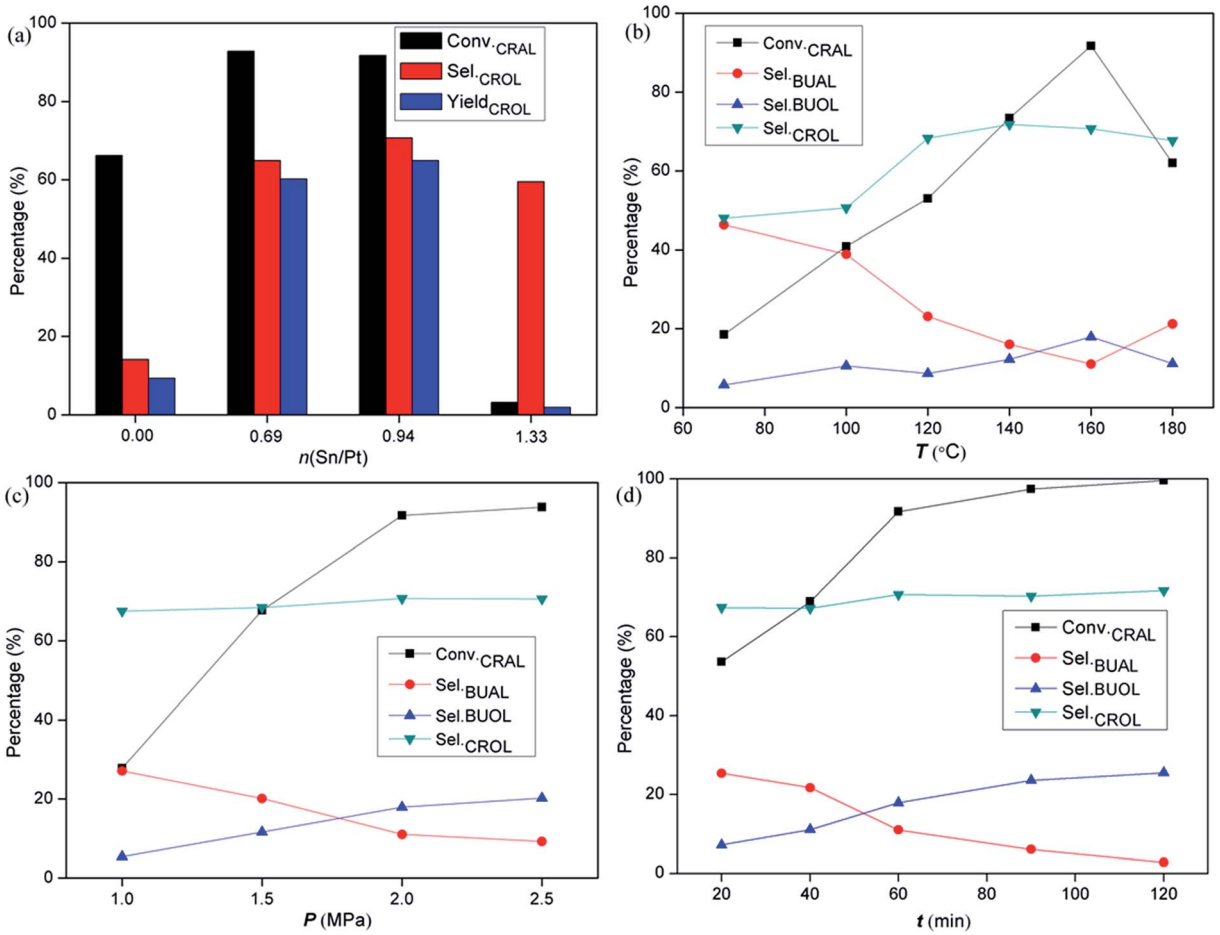

Fig. 8 (a) Liquid phase hydrogenation results over the $PtSn_x$/LOC catalysts with different Sn/Pt molar ratios. Reaction conditions: 1 mL CRAL catalyzed by 100 mg of the catalyst in 19 mL ethanol, $T = 160$ °C, $p = 2.0$ MPa, $t = 60$ min. Liquid phase hydrogenation results of CRAL over the $PtSn_{0.94}$/LOC as a function of: (b) temperature, (c) H_2 pressure and (d) time.

with the desorbed hydrogen/CO capacity determined by H_2-TPD and CO-DRIFT analyses, which most likely result from the composition-dependent variations in the exposure degree of active Pt sites and the interaction between carbonyl groups and Pt centers. By contrast, as shown in Table S1,† the selectivity to crotyl alcohol (62.0%) at a conversion of 81.2% is obtained on $PtSn_{0.94}$/LOC-CI, and the value is decreased to 54.3% at a conversion of 79.6% for $PtSn_{0.94}$/LOC-NP, much lower than that obtained on the $PtSn_{0.94}$/LOC, highlighting the superiority of $La_2O_2CO_3$ nanorods and sonochemical approach in this work.

Reaction parameters, *e.g.* hydrogen pressure, temperature and time, can affect the kinetics of competitive adsorption and hydrogenation of the reactant. Reaction parameters are tested

in order to evaluate their influence on the activity and selectivity for liquid-phase CRAL hydrogenation. Reaction parameters have been optimized by correlating reaction rates with product distributions over the $PtSn_{0.94}$/LOC. As can be seen from Fig. 8b, high hydrogenation rate is attainable with increasing reaction temperature, mainly from the formation of alcohol products coupled with a decreased yield of saturated aldehyde. In a period reaction of 60 min, the CROL selectivity presents a "parabola" curve: it ascends to 71.5% as the temperature rises to 160 °C, and then descends slightly at higher temperature possibly due to the distortion of the catalyst structure. When reaction temperature is 160 °C, increasing hydrogen pressure and reaction time displays an analogous promotion effect on the reactivity, while the CROL selectivity retains at the initial level (around 70%) with additional formation of BUOL, resulting from the deep hydrogenation of BUAL. Noticeably, an optimization of Sn content and reaction conditions gives rise to a 1.5-fold and 5-fold improvement in reactivity and CROL selectivity over the Pt/LOC. The extremely high activity and CROL selectivity over the $PtSn_{0.94}$/LOC clearly demonstrate that the coexistence of Pt and the partially reduced SnO_x species is essential to achieve high efficiency in carbonyl hydrogenation.

3.2.2 Recyclability of the catalysts. Recyclability is one of the most vital parameters for the evaluation of heterogeneous catalysts. It is known that the liquid-phase hydrogenation process produces not only the main products, but also the by-products from condensation reaction. In our test, trace amount of acetals and hemiacetals (total amount below 5%) is detected, usually covering on or even poisoning the catalytic active sites. Therefore, calcination at 300 °C in air for 1 h is adopted as a treatment to regenerate the used catalysts for characterizations or cycle experiment. Fig. S2† shows the hydrogenation results of CRAL on the selected Pt/LOC and $PtSn_{0.94}$/LOC during 5 runs. It is found that no significant decrease in reactivity occurs on the Pt/LOC and the CROL selectivity increases from 13.8% to 24.6%. By contrast, the reactivity over the $PtSn_{0.94}$/LOC vibrates around 90% during the first 3 cycles, after which an evident deactivation is observed but the CROL selectivity still remains above 60%.

To explore the reason for catalyst deactivation, characterizations including XRD patterns, HAADF-STEM images and XPS spectra on the cycled catalysts (denoted as Pt/LOC-C and $PtSn_{0.94}$/LOC-C) are elaborately performed. As shown in Fig. S3,† the diffraction patterns of the cycled catalysts can be indexed to hexagonal $La_2O_2CO_3$ (JCPDS No. 25-0424). HAADF-STEM images in Fig. S4† reveal that the cycled catalysts consist of highly dispersed metal NPs with narrow size distributions, which can explain why no diffraction signals related to metals are detected. The almost unchanged Pt particle size of Pt/LOC-C relative to the Pt/LOC, provide direct evidence that the working catalyst is rather stable probably due to the strong anchoring sites on the lanthanum surfaces, which inhibits the migration and growth of Pt atoms even after five reduction–oxidation cycles. While for $PtSn_{0.94}$/LOC-C, an obvious increase in metal particle size is observed, showing an average size of 2.2 nm, higher than that for $PtSn_{0.94}$/LOC (1.3 nm).

As is clear from XPS analyses in Fig. S5 and Table S2,† Pt in the cycled catalysts still exists as a mixture of Pt^0 and Pt^{2+}, showing a higher Pt^{2+}/Pt^0 value than the fresh ones presumably resulting from calcinations in air to regenerate the catalysts. No metallic tin is detected for $PtSn_{0.94}$/LOC-C and tin exists as ionic states (Sn^{2+} or Sn^{4+}), suggesting a complete phase segregation of PtSn alloys. In addition, the Sn/Pt value of $PtSn_{0.94}$/LOC-C is much lower than the fresh one, implying that a small amount of tin species leaches out during the reaction process. According to the previously discussed XRD and XPS results, the decreased phase composition of La_2O_3 for fresh $PtSn_{0.94}$/LOC compared to the Pt/LOC clearly illustrates that the tin addition much weakens the Pt–lanthanum interfaces, resulting into more Pt atoms segregated from lanthanum surfaces to interact with the tin species. Therefore, it is plausible that the heat-treatment in air can easily induce the phase segregation of PtSn alloys and further result into the loss of SnO_x layers, assuming that a weak interaction between lanthanum and tin oxides.[43] Moreover, ICP-OES results in Table S2† clearly indicate a decrease of Sn content (0.46 wt%) and Sn/Pt molar ratio (0.73) in $PtSn_{0.94}$/LOC-C compared to the fresh $PtSn_{0.94}$/LOC, which provides further evidence on the leaching of Sn during the cycle experiment. Above results lead us to a conclusion that the phase segregation of PtSn alloys and the loss of SnO_x patches in the vicinity of Pt centers during the cycle experiments, may be the primary reason responsible for the catalyst deactivation of the $PtSn_{0.94}$/LOC.

4. Discussion

According to the reactive performance over the resultant catalysts, bimetallic PtSn systems are highly active and selective for CRAL hydrogenation to the desired CROL compared to the parent Pt/LOC. It seems that the enhanced catalytic behaviors of tin-modified catalysts most likely result from the interaction between Pt and the tin species, which affects the Pt–support interfaces and the bimetallic structure. Therefore, it is worthwhile to study the interaction between both metals and lanthanum surfaces on the basis of detailed characterization data.

4.1 Pt–lanthanum interfaces

The electronic and structural properties of the Pt/LOC are estimated to probe the metal–support interaction. XRD patterns in Fig. 1 suggest that Pt atoms onto the lanthanum surfaces catalyze the phase transformation of $La_2O_2CO_3$ to La_2O_3, which is supported by the variations of La 3d spectra in Fig. 3d. As shown in Fig. 3a, the split of Pt 4f spectra into metallic Pt^0 and oxidized Pt^{2+} clearly demonstrates that two kinds of platinum species coexist in the catalyst. On account of the high-temperature reduction, Pt^{2+} species can be ascribed to Pt atoms that are strongly interacted with lanthanum through the Pt–O–La bond. The Pt–O contribution to the Pt L_{III}-edge EXAFS oscillation provide further evidence on the existence of O-coordinated Pt atoms at the Pt–lanthanum interfaces. On one hand, the strong metal–support interaction (SMSI) plays a decisive role in retaining the high platinum dispersion even

after reduction at 600 °C (see Fig. 2), further inhibiting the metal sintering during the cycle experiment (see Fig. S4†). On the other hand, this SMSI effect usually decreases the exposure degree of Pt sites, since it produces Pt atoms partially embedded by oxides patches. Analogous phenomenon has been discussed in other studies on the Pt doped ceria surfaces.[35,44]

As introduced into the Pt/LOC, the tin species can be randomly dispersed on the support surface or located in the vicinity of Pt atoms. TEM images of tin-promoted samples in Fig. 2 show that no obvious changes in the metal particle size were observed upon the tin addition, hence we can discuss the composition-dependent properties of the PtSn catalysts while excluding the particle size effect. A decreasing Pt^{2+}/Pt^0 values and the reducing CN values of Pt–O contribution for tin-modified catalysts reveal that the reducibility of platinum is greatly improved possibly owing to the crippling Pt–lanthanum interfaces after the decoration of tin, which is validated by an increase in metal particle size of tin-dopped catalysts during cycle experiment. As indicated by XRD analyses in Fig. 1, introducing a limited quantity of tin results into an increase in the phase composition of La_2O_3, while an opposite trend is observed when Sn/Pt ratio $\geq$ 0.94. These results suggest two different modification effects of tin on the Pt–lanthanum interfaces depending on the Sn/Pt ratios. At low Sn content, the dilution effect of Pt by tin predominates and produces individual Pt atoms segregated from lanthanum surfaces; whereas at high Sn content, more Pt atoms are interacted with the tin species and the passivation effect of tin on the catalyst surface prevails.

4.2 Bimetallic particles

The interaction between Pt and the tin species is estimated by XPS, CO-DRIFT and XAS techniques. The Pt–Sn contributions to the Pt L_{III}-edge oscillation confirm the dilution of Pt atoms by PtSn alloys or SnO_x species. XPS characterization manifests that the number of the O-coordinated Pt atoms is greatly decreased accompanied by a limited quantity of metallic Sn^0 when Sn/Pt ratio $\geq$ 0.94, suggesting the generation of Pt–SnO_x entities at high Sn loading.

In the case of small particles (particle size below 50 Å), the composition-dependent structural changes are reflected in varying CNs of the scattering paths from central atom.[9,18] The Pt–O, Pt–Pt and Pt–Sn contributions in the curve fitting of Pt L_{III}-edge provide further information on the bimetallic structure. The average CN of the Pt–Sn shell for $PtSn_{0.69}$/LOC is 1.1, and this value is decreased to 0.3 for $PtSn_{0.94}$/LOC and 0.2 for $PtSn_{1.33}$/LOC, most likely resulting from the phase segregation of PtSn alloys.[41] Meanwhile, the shorter distances of Pt–Pt bond for $PtSn_{0.94}$/LOC and $PtSn_{1.33}$/LOC than that for Pt/LOC and $PtSn_{0.69}$/LOC, suggests a contraction of the interatomic distance due to the formation of small Pt clusters possibly segregated from PtSn alloys. These EXAFS fitting results give a clear illustration on the possible structure evolution of bimetallic NPs from SnO_x-patched PtSn alloys to SnO_x-patched Pt clusters with increasing Sn/Pt ratios. Besides, the CN value of Pt–O contribution to the $PtSn_{1.33}$/LOC is decreased to 1.0 with respect to the Pt/LOC (1.5). In addition to the decreased O/La ratio from XPS analyses, it is suggested that surface oxygenic species are partially consumed at high Sn loading. One plausible reason is that surface oxygen vacancy sites are generated, presumably due to the reduction of Pt–SnO_x sites through electron capture and transfer upon hydrogen spillover.[41,45]

From these results we can conclude that bimetallic samples are composed of O-coordinated Pt^{2+} atoms and Pt^0 clusters, which are diluted by the PtSn alloys and SnO_x species. Although most of tin cannot be reduced to metallic form and incorporated into an alloy, it affects the geometric structure of platinum and helps to stabilize the Pt atoms. Furthermore, the composition-dependent changes in bimetallic structure are proposed to account for the distinct catalytic behavior.

4.3 The correlations between structure evolution and catalytic behavior

The above results reflect an interaction between Pt and Sn, which is related to the formed PtSn alloys and Pt–SnO_x species. Such an interaction exerts a great influence on the reaction route. The product distribution demonstrates that the reaction proceeds through preferential hydrogenation of C=O bond for bimetallic system. In particular, over the $PtSn_{0.94}$/LOC, the selectivity and yield to CROL achieves a 5-fold and 7-fold improvement over the Pt/LOC. Additionally, $PtSn_{0.94}$/LOC retains its selectivity at the initial level (around 70%), irrespective of the reaction time and hydrogen pressure.

It seems reasonable to accept that the enhanced carbonyl selectivity of bimetallic system is originated from the intrinsic nature of Pt, as our tests show that tin oxides are inactive for CRAL hydrogenation and participate only in the isolation of Pt atoms. It is proposed that the chemisorption behaviors of H_2 and CO on metal sites originate from the interacting surfaces of Pt and Sn at the atomic level.[41] The H_2-TPD and CO-DRIFT measurements are employed to extract the correlation between the bimetallic structure and the catalytic behavior. It is found that incorporating a small amount of tin (Sn/Pt ratio equals to 0.69) substantially increases the number of active Pt sites for hydrogen, presumably due to the prevailing effect of site isolation generated by tin. Meanwhile, this dilution effect favors the reversible adsorption of linear Pt–CO, which is accounted for the improvement in hydrogenation rate for $PtSn_{0.69}$/LOC compared to the Pt/LOC. However, when Sn/Pt ratio $\geq$ 0.94, excessive tin results into the passivation effect of the catalyst surface and greatly reduce the exposure of Pt sites for H_2 and CO adsorption. Besides, the interaction between CO and Pt is greatly enhanced with increasing Sn loadings, as evidenced by the red-shift of linear Pt–CO band and the desorption behavior from CO-DRIFTS spectra. This increased interaction plays a decisive role in the competitive adsorption and hydrogenation of carbonyl groups, whereas lowers the desorption rate of the products and hinders the recovery of active sites. Consequently, the hydrogenation rate of CRAL is sharply decreased at high Sn loadings.

It is known that the hydrogenation product of unsaturated aldehyde is strongly dependent on the adsorption mode of

reactant molecule on the catalyst surface.[37,46] According to the reactive performance over the prepared catalysts, two possible adsorption models of CRAL over the prepared Pt and PtSn catalysts are proposed. On the Pt/LOC, the support effect is the primary factor for the selective hydrogenation. The carbonyl oxygen is suggested to interact with the positively charged Pt^{2+}, and the Pt^0 site is the adsorption center of C=C bond. In this model, the hydrogenation of C=C and C=O bonds is competitive, which dominates the selectivities to BUAL and CROL, respectively. While for tin-promoted catalysts, additional Pt–SnO_x sites are generated onto the catalyst surface. The carbonyl group could chemisorb on the Pt–SnO_x entities through the carbonyl carbon with the Pt^0 site and carbonyl oxygen with electropositive Sn^{n+} species to form a di-σ_{CO} adsorption mode, which is proposed to facilitate the polarization and activation of the C=O bond.[21,38] Evidently, the activation of the C=O bond on the Pt–SnO_x entity is much easier than that on the Pt^0–Pt^{2+} couple, which accounts for the additional activity attained on the tin-modified catalysts compared to the Pt/LOC. In addition, oxygen vacancies related to the generation of Pt–SnO_x entities is evidenced by the XPS and EXAFS-fitting results. This improved Pt–SnO_x couple is likely to further enhance the selective activation and hydrogenation of C=O bond.

By analyzing the activity of PtSn/LOC catalysts as a function of the Sn/Pt ratios, there seems to be a dilution effect of Pt sites, yielding higher hydrogenation rates for reaction, and a promoting effect of ionic Sn, favoring the preferential hydrogenation for carbonyl groups.[21,34] However, excessive tin loading in the bimetallic catalysts drastically reduces the conversion rate of CRAL. Therefore, the synergy between Pt sites and tin species leads to an optimum Sn/Pt ratio.

5. Conclusion

In summary, liquid-phase CRAL hydrogenation is used as a model reaction to test the tin-promoted Pt/LOC catalysts, which are highly selective to the desired unsaturated alcohol compared to the Pt/LOC. The strong metal–support interaction in the Pt/LOC plays an important role in retaining high dispersion of Pt, giving rise to a good reproducibility during cycle experiment. For bimetallic systems, the distinct reactive performance can be tentatively attributed to the composition-dependent structure of bimetallic particles. The varying Sn/Pt ratios determine the atomic arrangement of bimetallic NPs and the geometric characteristics of Pt, which dominates the adsorption mode of CRAL molecules and is proposed to be accounted for the additional activity towards carbonyl hydrogenation. However, the $PtSn_{0.94}$/LOC easily suffers from the catalyst deactivation due to the phase segregation of PtSn alloys and the leaching effect of SnO_x patches. This work demonstrates that high performing catalysts with both metals can be achieved by adjustment of the bimetallic structure, and provides a further understanding on the fabrication of bimetallic catalysts for specific heterogeneous reaction.

Conflicts of interest

There are no conflicts to declare.

Acknowledgements

Sincere acknowledge is made to the financial support from the National Science Foundation of China (21401204), Innovation Promotion Association CAS (2017460), the Western Light Program of Chinese Academy of Sciences (2015), and Science and Technology Project of Suzhou City (SYG201627). The X-ray absorption spectroscopy is granted by 4W1B station of Beijing Synchrotron Radiation Facility, Institute of High Energy Physics, Chinese Academy of Sciences. The staff members of 4W1B are acknowledged for their support in measurements and data reduction.

References

1 P. Gallezot and D. Richard, *Catal. Rev.*, 1998, **40**, 81–126.
2 X. Yang, A. Wang, X. Wang, T. Zhang, K. Han and J. Li, *J. Phys. Chem. C*, 2009, **113**, 20918–20926.
3 M. Abid, V. Paul-Boncour and R. Touroude, *Appl. Catal., A*, 2006, **297**, 48–59.
4 A. Dandekar and M. A. Vannice, *J. Catal.*, 1999, **183**, 344–354.
5 H. Yoshitake and N. Saito, *Microporous Mesoporous Mater.*, 2013, **168**, 51–56.
6 H.-Y. Chen, C.-T. Chang, S.-J. Chiang, B.-J. Liaw and Y.-Z. Chen, *Appl. Catal., A*, 2010, **381**, 209–215.
7 P. Reyes, H. Rojas and J. L. G. Fierro, *Appl. Catal., A*, 2003, **248**, 59–65.
8 X. Yang, Y. Mueanngern, Q. A. Baker and L. R. Baker, *Catal. Sci. Technol.*, 2016, **6**, 6824–6835.
9 A. Siani, O. S. Alexeev, G. Lafaye and M. D. Amiridis, *J. Catal.*, 2009, **266**, 26–38.
10 I. M. J. Vilella, S. R. de Miguel and O. A. Scelza, *J. Mol. Catal. A: Chem.*, 2008, **284**, 161–171.
11 I. M. Vilella, I. Borbáth, J. L. Margitfalvi, K. Lázár, S. R. de Miguel and O. A. Scelza, *Appl. Catal., A*, 2007, **326**, 37–47.
12 F. Coloma, J. Llorca, N. Homs, P. R. de la Piscina, F. Rodriguez-Reinoso and A. Sepulveda-Escribano, *Phys. Chem. Chem. Phys.*, 2000, **2**, 3063–3069.
13 J. Shi, M. Zhang, W. Du, W. Ning and Z. Hou, *Catal. Sci. Technol.*, 2015, **5**, 3108–3112.
14 Z. Tian, C. Liu, Q. Li, J. Hou, Y. Li and S. Ai, *Appl. Catal., A*, 2015, **506**, 134–142.
15 W. O. Oduro, N. Cailuo, K. M. K. Yu, H. Yang and S. C. Tsang, *Phys. Chem. Chem. Phys.*, 2011, **13**, 2590–2602.
16 H. Rong, Z. Niu, Y. Zhao, H. Cheng, Z. Li, L. Ma, J. Li, S. Wei and Y. Li, *Chem.–Eur. J.*, 2015, **21**, 12034–12041.
17 S. T. Christensen, H. Feng, J. L. Libera, N. Guo, J. T. Miller, P. C. Stair and J. W. Elam, *Nano Lett.*, 2010, **10**, 3047–3051.
18 G. J. Siri, J. M. Ramallo-López, M. L. Casella, J. L. G. Fierro, F. G. Requejo and O. A. Ferretti, *Appl. Catal., A*, 2005, **278**, 239–249.
19 F. Coloma, A. Sepúlveda-Escribano, J. L. G. Fierro and F. Rodríguez-Reinoso, *Appl. Catal., A*, 1996, **136**, 231–248.

20 J. P. Stassi, P. D. Zgolicz, V. I. Rodríguez, S. R. de Miguel and O. A. Scelza, *Appl. Catal., A*, 2015, **497**, 58–71.
21 J. P. Stassi, P. D. Zgolicz, S. R. de Miguel and O. A. Scelza, *J. Catal.*, 2013, **306**, 11–29.
22 A. Huidobro, A. Sepúlveda-Escribano and F. Rodríguez-Reinoso, *J. Catal.*, 2002, **212**, 94–103.
23 A. B. da Silva, E. Jordão, M. J. Mendes and P. Fouilloux, *Appl. Catal., A*, 1997, **148**, 253–264.
24 Y.-H. Hou, W.-C. Han, W.-S. Xia and H.-L. Wan, *ACS Catal.*, 2015, **5**, 1663–1674.
25 T. Levan, M. Che, J. M. Tatibouet and M. Kermarec, *J. Catal.*, 1993, **142**, 18–26.
26 W. Gu, J. Liu, M. Hu, F. Wang and Y. Song, *ACS Appl. Mater. Interfaces*, 2015, **7**, 26914–26922.
27 X. Huang, C. Dang, H. Yu, H. Wang and F. Peng, *ACS Catal.*, 2015, **5**, 1155–1163.
28 L. Jin, Y. Zhang, J. P. Dombrowski, C.-H. Chen, A. Pravatas, L. Xu, C. Perkins and S. L. Suib, *Appl. Catal., B*, 2011, **103**, 200–205.
29 Y. Zhang, L. Jin, K. Sterling, Z. Luo, T. Jiang, R. Miao, C. Guild and S. L. Suib, *Green Chem.*, 2015, **17**, 3600–3608.
30 F. Hou, H. Zhao, J. Zhao, J. Yang, L. Yan, H. Song and L. Chou, *J. Nanopart. Res.*, 2016, **18**, 1–17.
31 B. Ravel and M. Newville, *J. Synchrotron Radiat.*, 2005, **12**, 537–541.
32 S. Irusta, L. M. Cornaglia and E. A. Lombardo, *Mater. Chem. Phys.*, 2004, **86**, 440–447.
33 K. S. Kim, N. Winograd and R. E. Davis, *J. Am. Chem. Soc.*, 1971, **93**, 6296–6297.
34 J. Shi, M. Zhang, W. Du, W. Ning and Z. Hou, *Catal. Sci. Technol.*, 2015, **5**, 3108–3112.
35 J. Lee, Y. Ryou, X. Chan, T. J. Kim and D. H. Kim, *J. Phys. Chem. C*, 2016, **120**, 25870–25879.
36 Y. Zhou, D. E. Doronkin, M. Chen, S. Wei and J.-D. Grunwaldt, *ACS Catal.*, 2016, **6**, 7799–7809.
37 J. Haubrich, D. Loffreda, F. Delbecq, P. Sautet, Y. Jugnet, C. Becker and K. Wandelt, *J. Phys. Chem. C*, 2010, **114**, 1073–1084.
38 K. Taniya, H. Jinno, M. Kishida, Y. Ichihashi and S. Nishiyama, *J. Catal.*, 2012, **288**, 84–91.
39 S.-H. Liu, F.-S. Zheng and J.-R. Wu, *Appl. Catal., B*, 2011, **108**, 81–89.
40 F. Behafarid, L. K. Ono, S. Mostafa, J. R. Croy, G. Shafai, S. Hong, T. S. Rahman, S. R. Bare and B. Roldan Cuenya, *Phys. Chem. Chem. Phys.*, 2012, **14**, 11766–11779.
41 H. Rong, Z. Niu, Y. Zhao, H. Cheng, Z. Li, L. Ma, J. Li, S. Wei and Y. Li, *Chem.–Eur. J.*, 2015, **21**, 12034–12041.
42 Z. Niu, N. Becknell, Y. Yu, D. Kim, C. Chen, N. Kornienko, G. A. Somorjai and P. Yang, *Nat. Mater.*, 2016, **15**, 1188–1194.
43 Y. Uemura, Y. Inada, K. K. Bando, T. Sasaki, N. Kamiuchi, K. Eguchi, A. Yagishita, M. Nomura, M. Tada and Y. Iwasawa, *Phys. Chem. Chem. Phys.*, 2011, **13**, 15833.
44 Y. Nagai, T. Hirabayashi, K. Dohmae, N. Takagi, T. Minami, H. Shinjoh and S. i. Matsumoto, *J. Catal.*, 2006, **242**, 103–109.
45 R. Prins, *Chem. Rev.*, 2012, **112**, 2714–2738.
46 F. Delbecq and P. Sautet, *J. Catal.*, 2002, **211**, 398–406.